An efficient, simple, and precise way to map strain with nanometer resolution in semiconductor devices

Christoph T. Koch, V. Burak Özdöl, and Peter A. van Aken

Additional information on Appl. Phys. Lett.

An efficient, simple, and precise way to map strain with nanometer resolution in semiconductor devices

Christoph T. Koch,[a] V. Burak Özdöl, and Peter A. van Aken

Max Planck Institute for Metals Research, D-70569 Stuttgart, Germany

We report on the development of the dark-field inline electron holography technique and its application to map strain in technologically relevant structures, using as an example the strain-engineered gate channel in a 45 nm metal-oxide semiconductor field-effect transistor structure. We show that this technique combines a large field of view of several micrometers with high precision (better than 0.01%), high spatial resolution (better than 1 nm), and very loose experimental requirements not possible with any other technique currently available. © *2010 American Institute of Physics*. [doi:10.1063/1.3337090]

The ability to measure local strain on the nanometer scale is an essential tool for characterizing modern nanostructured materials. Local stress fields affect materials mechanical and electronic properties, may induce diffusion, or control mass transport during growth, being responsible, for example, for self-organization and growth of quantum dots. Strain-induced alteration of the band structure in semiconductors is being utilized for increasing the mobility of charge carriers in modern metal-oxide semiconductor field-effect transistor (MOSFET) and dynamic random access memory structures and with that the device performance.[1,2] Being able to map strain with high spatial resolution and a large field of view of at least 1 μm is therefore crucial for developing modern microelectronic devices. Here we present a simple method for measuring the two-dimensional strain tensor with high precision, a large field of view, and better than 1 nm spatial resolution. This method can be applied on any standard transmission electron microscope (TEM) and minimizes electron dose on the investigated specimen.[3]

Among all kinds of radiation being used to measure strain, i.e., neutrons,[4] x-rays,[5] electrons,[6–10] or light,[11] electron scattering based techniques, because of the small wavelength and high scattering strength of electrons, and the possibility to focus them into small volumes, offer the highest spatial resolution. Within the field of electron scattering techniques applied for strain mapping, real-space methods relying on the analysis of the phase shift of scattered electron wave functions, namely, the geometric phase analysis (GPA) of high-resolution transmission electron microscopy (HRTEM) images[9] or dark-field off-axis holography (DOAH),[10,12] offer generally a higher spatial resolution than methods analyzing the geometric distortions in local diffraction patterns.[6–8]

The dark-field inline holography (DIH) method presented in this letter also relies on data collected in real space, but, in contrast to HRTEM-GPA or DOAH does not derive the strain information from the position of interference fringes of the scattered electron wave, but instead from variations in the intensity of dark-field TEM images with defocus. The resulting non-necessity to sample fine interference fringes at a sufficiently high magnification allows for optimum use of the number of pixels in the detector and severely reduces the sensitivity to detector distortions which almost invariably occur in today's fiber-optically coupled charge coupled device (CCD) detectors. Also, in contrast to DOAH, the DIH strain mapping technique introduced here has virtually no requirements on the spatial coherence of the illuminating electron beam,[13] making it much more widely applicable.

Figure 1 shows the experimental setup and contrast mechanism that is being made use of in DIH. Diffraction-based techniques[4–8] analyze tiny shifts in the diffraction plane [strongly exaggerated in Fig. 1(a)] while scanning a (small) probe relative to the sample. Such shifts in reciprocal space are caused by local lattice distortions and with that changes in scattering angle and correspond to a phase shift in real space. According to the diagram shown in Fig. 1(a), because of the tilted illumination the transmitted beam ($\vec{k}_0$) is blocked by the objective aperture located in the back-focal
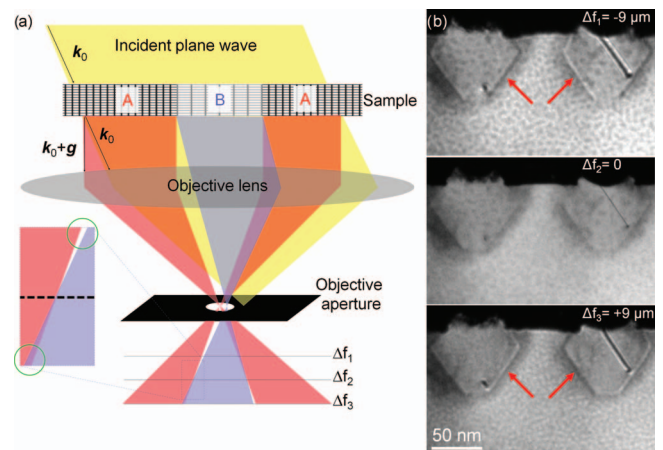

FIG. 1. (Color) (a) Diagram illustrating the principle of DIH. A diffracted beam $\vec{g}$ is selected using the objective aperture and dark-field images for at least three different planes of defocus ($\Delta f_1, \ldots, \Delta f_3$) are recorded. Lattice distortions (indicated by regions of different lattice constant A and B) lead to locally varying diffracting conditions and produce bright and dark features in places where the diffracting condition changes, as highlighted by the green circles in the inset. (b) Experimental dark-field inline holograms of a p-MOSFET structure. At the boundaries of regions of different lattice constant, i.e., SiGe (in the source and drain—see Fig. 2) and Si (in the substrate and also the gate channel), bright and dark bands (highlighted by red arrows) appear as illustrated in (a).
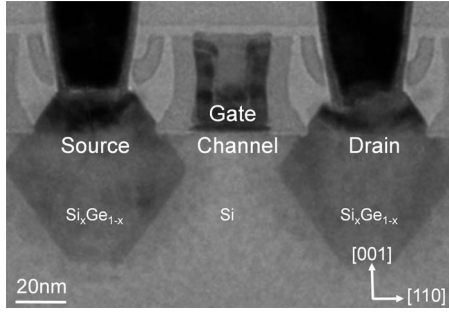
[a]Electronic mail: koch@mf.mpg.de.

FIG. 2. Bright-field image of the 45 nm technology p-MOSFET structure of a commercial processor used for the work presented here. The individual transistor components are labeled. The thin TEM samples have been prepared conventionally, i.e., by cutting a thin slice from a commercial processor and mechanically grinding it using a tripod polisher (AlliedTech). The resulting wedge-shaped sample was then polished using a beam of argon ions accelerated at low voltages (500 V) while cooling the sample to liquid Nitrogen temperature (Fischione, Model 1010).

plane of the objective lens (diffraction plane) positioned on the optic axis of the microscope. By proper choice of the tilt angle different diffracted beams $(\vec{k}_0+\vec{g})$ can be aligned with the optic axis of the microscope. The only difference to conventional dark-field imaging is that we now record images at least three different planes of defocus. Figure 1(b) shows subareas of three differently focused (220) dark-field images of a 45 nm p-MOSFET structure (see Fig. 2 for a bright-field image) recorded on the Sub-Electron-Volt-Sub-Angstrom-Microscope (SESAM) (Ref. 14) (Carl Zeiss NTS) using a 2k×2k fiber-optically coupled UltraScan™ 1000 CCD camera (Gatan, Inc.). The SESAM's in-column Mandoline filter was used for removing the contribution of inelastically scattered electrons to the recorded dark-field images. Defocus values of $\Delta f_1 = -9$ μm, $\Delta f_2 = 0$ μm, and $\Delta f_3 = +9$ μm were achieved by varying the objective lens current. This task of recording a focal series is fully automated on most TEMs. An objective aperture with a diameter of 10 μm has been used to limit the resolution of these images to 0.77 nm. The in-focus ($\Delta f_2 = 0$) dark-field image provides the local intensity of the diffracted electron beam.

For small changes in defocus the corresponding phase of the diffracted electron wave function may be determined from a finite difference approximation of the transport of intensity equation (TIE) (Ref. 15)

$$\nabla_\perp^2 \phi_{\vec{g}}(\vec{r}) = \frac{-2\pi}{\lambda} \nabla_\perp \left[\frac{1}{I(\vec{r})} \nabla_\perp \frac{\partial I(\vec{r})}{\partial \Delta f} \right]$$
$$\approx \frac{-2\pi}{\lambda} \nabla_\perp \left[\frac{1}{I_2(\vec{r})} \nabla_\perp \frac{I_3(\vec{r}) - I_1(\vec{r})}{\Delta f_3 - \Delta f_1} \right], \quad (1)$$

where $I_n(\vec{r})$ is the intensity of the dark-field image at defocus Δf_n. Within the column approximation (see also Ref. 16 for a discussion of the effect of this approximation on the phase and amplitude of diffracted beams) and in absence of variations in local crystal structure or diffracting condition the phase $\phi_{\vec{g}}(\vec{r})$ of the diffracted wave function is equal to the geometric phase $\phi_{\mathrm{geom}}(\vec{r})$.[9,10]

$$\phi_{\mathrm{geom}}(\vec{r}) = 2\pi[\vec{g}(\vec{r}) - \vec{g}_0] \cdot \vec{r} = 2\pi \vec{g}_0 \cdot \Delta \vec{r}(\vec{r}), \quad (2)$$

where $\vec{g}_0$ is the reciprocal lattice vector at the center of the objective aperture, $\vec{g}(\vec{r})$ the lattice vector corresponding to the local lattice parameters, and $\Delta \vec{r}(\vec{r})$ the local displacement

field, i.e., the shift of the local unit cell with respect to a global reference lattice with lattice vector $\vec{g}_0$.[9]

In places where the strain state of the sample changes, i.e., where we have variations in the strain

$$\epsilon_{i,j}(\vec{r}) = \frac{\partial \Delta \vec{r}(\vec{r})_i}{\partial \vec{r}_j}, \quad (3)$$

the Laplacian of the geometric phase $\nabla_\perp^2 \phi_{\mathrm{geom}}(\vec{r})$ and with that the change in image intensity with defocus are nonzero which can easily be seen by comparing the dark-field images shown in Fig. 1(b).

In case the change in defocus Δf between images is large, as in the case presented here, very small details in the geometric phase obtained by the TIE [expression (1) with subsequent application of the inverse Laplace operator] will not be accurately reconstructed. We have therefore applied a combined approach[17] which corrects high-resolution inaccuracies in the TIE reconstruction by refining the initial TIE result using a nonlinear reconstruction algorithm.[13,18] This algorithm also correctly treats partial spatial coherence of the illuminating wave function. The resulting geometric phase is shown in Fig. 3(a). Since this approach reconstructs the phase of the diffracted wave function directly, no phase wrapping is involved, which is why the phase in Fig. 3(a) is presented on a gray scale of $-5\pi, \ldots, 5\pi$.

The reconstruction of the two-dimensional strain tensor requires the geometric phase maps of two[9,10] or more[19] noncolinear reflections and has already become a standard procedure. For the p-MOSFET structures investigated in this report only the lateral strain component ϵ_{xx} along the (220) direction was of major interest because of its effect on the charge carrier mobility within the gate channel. If only a single component of the strain tensor is required, it suffices to record dark-field inline holograms only for a reflection along the direction of interest. We have therefore restricted ourselves to present here only experimental data for the (220) reflection required to reconstruct the horizontal strain component ϵ_{xx}, as shown in Fig. 3(b).

While the dark-field images used for reconstructing the strain map in Fig. 3(b) [see Fig. 1(b) for subregions of three of these images] have been sampled using a pixel size of 0.58 nm (24 000 times magnification at a CCD pixel size of 14 μm) the successful application of the GPA of HRTEM images requires a sampling at least ten times as fine, requiring a 100 times higher electron dose on the sample in order to achieve the same number of counts per pixel. In addition, the contrast of lattice fringes in HRTEM images is very often less than 10% (Ref. 20) which requires an even higher electron dose, in order to achieve signal-to-noise properties sufficient for producing high-precision displacement maps. The lattice-resolution HRTEM image shown in the inset in Fig. 3(b) has been recorded at the JEOL ARM1250 high-voltage TEM (resolution: 0.11 nm)[21] on photographic film and was then digitized using a 2k×2k CCD camera with a spatial sampling of 0.058 nm. The number of detector pixels was the same as for the low resolution images (2048×2048 pixels) so that the ten times higher spatial sampling results in a field of view of only 0.1×0.1 μm², i.e., only 1/10th of that of the dark-field images. However, the strain profiles presented in Fig. 3(c) show that a field of view of at least 0.2 μm is necessary to include both the gate channel as well as a (narrow) reference area of undistorted perfect crystal. Also, the
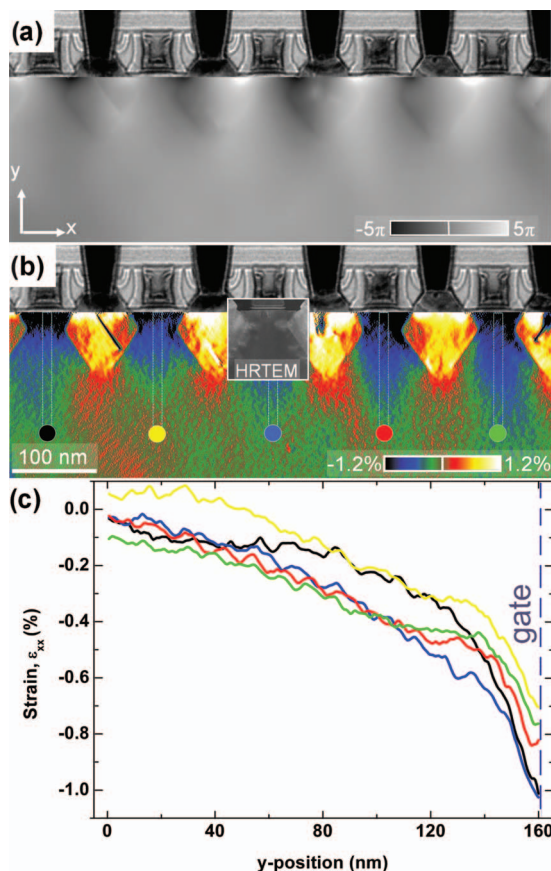
FIG. 3. (Color) (a) Geometric phase reconstructed from a focal series of 15 dark-field inline electron holograms for the (220) reflection. The defocus step fitted by the FULL-RESOLUTION WAVE RECONSTRUCTION software (Ref. 18) was 3.98 μm. Above the phase map a bright-field image of the contacts is shown. (b) Map of the ϵ_{xx} strain component extracted from the geometric phase map shown in (a). The gate channels are compressively strained. As in (a), a bright-field image showing the electrical contacts is shown above the strain map. The inset shows a 2k×2k pixel HRTEM image recorded with the largest possible field of view (0.1×0.1 μm^2) to still allow applying GPA. (c) Vertical strain profiles extracted from the narrow boxes in the ϵ_{xx} map shown in (b). The color of each plot corresponds to the color of the dot in (b) defining the line profile's origin. The profiles have been averaged across the width of the 11.7 nm (20 pixels) wide boxes shown in (b).

large electron dose, aided possibly by the high electron beam energy of 1250 keV, seems to have triggered strain-induced diffusion of Ge from the source and drain into the surrounding silicon crystal. This effect could not be observed in any of the images recorded at lower magnification, demonstrat-

ing the fact that strain mapping by DIH is much more suitable for beam sensitive materials than GPA of HRTEM images.

While it is quite obvious that the electron dose requirements of strain mapping by DIH are much lower than for HRTEM-GPA they are also much lower than for DOAH. In addition to the much simpler experimental setup of inline holography compared to off-axis holography, the inline technique has the additional advantage of being able to freely adjust the signal-to-noise ratio independent of exposure time or illumination conditions. Since the signal is produced by variation of the image intensity with defocus, high-precision strain maps may be extracted from noisy low-dose data by choosing a large defocus step.[13]

[1]ITRS, International Technology Roadmap for Semiconductors, 2007 edition, http://www.itrs.net/reports.html.
[2]M. Chu, Y. Sun, U. Aghoram, and S. E. Thompson, Annu. Rev. Mater. Res. **39**, 203 (2009).
[3]T. M. Smeeton, M. J. Kappers, J. S. Barnard, M. E. Vickers, and C. J. Humphreys, Appl. Phys. Lett. **83**, 5419 (2003).
[4]A. Krawitz and T. M. Holden, MRS Bull. **15**, 57 (1990).
[5]E. J. Mittemeijer and U. Welzel, Z. Kristallogr. **223**, 552 (2008).
[6]A. J. Wilkinson, G. Meaden, and D. J. Dingley, Ultramicroscopy **106**, 307 (2006).
[7]P. Zhang, A. A. Istratov, E. R. Weber, C. Kisielowski, H. He, C. Nelson, and J. C. H. Spence, Appl. Phys. Lett. **89**, 161907 (2006).
[8]K. Usuda, T. Numata, T. Irisawa, N. Hirashita, and S. Takagi, Mater. Sci. Eng., B **124-125**, 143 (2005).
[9]M. J. Hÿtch, E. Snoeck, and R. Kilaas, Ultramicroscopy **74**, 131 (1998).
[10]M. J. Hÿtch, F. Houdellier, F. Hüe, and E. Snoeck, Nature (London) **453**, 1086 (2008).
[11]I. De Wolf, J. Raman Spectrosc. **30**, 877 (1999).
[12]K.-J. Hanszen, J. Phys. D: Appl. Phys **19**, 373 (1986).
[13]C. T. Koch and A. Lubk, "Off-axis and inline electron holography: A quantitative comparison," Ultramicroscopy (to be published).
[14]C. T. Koch, W. Sigle, R. Höschen, M. Rühle, E. Essers, G. Benner, and M. Matijevic, Microsc. Microanal. **12**, 506 (2006).
[15]M. R. Teague, J. Opt. Soc. Am. **73**, 1434 (1983).
[16]A. Howie and C. H. Sworn, Philos. Mag. **22**, 861 (1970).
[17]T. E. Gureyev, Opt. Commun. **220**, 49 (2003).
[18]C. T. Koch, Ultramicroscopy **108**, 141 (2008).
[19]A. K. Gutakovskii, A. L. Chuvilin, and S. A. Song, Bull. Russ. Acad. Sci. Phys. **71**, 1426 (2007).
[20]M. J. Hÿtch and M. Stobbs, Ultramicroscopy **53**, 191 (1994).
[21]F. Phillipp, R. Höschen, M. Osaki, G. Möbus, and M. Rühle, Ultramicroscopy **56**, 1 (1994).